

## Anharmonicity in bcc refractory elements

### A detailed ab initio analysis

Srinivasan, Prashanth; Shapeev, Alexander; Neugebauer, Jörg; Körmann, Fritz; Grabowski, Blazej

**DOI**

[10.1103/PhysRevB.107.014301](https://doi.org/10.1103/PhysRevB.107.014301)

**Publication date**

2023

**Document Version**

Final published version

**Published in**

Physical Review B

**Citation (APA)**

Srinivasan, P., Shapeev, A., Neugebauer, J., Körmann, F., & Grabowski, B. (2023). Anharmonicity in bcc refractory elements: A detailed ab initio analysis. *Physical Review B*, 107(1), Article 014301. <https://doi.org/10.1103/PhysRevB.107.014301>

**Important note**

To cite this publication, please use the final published version (if applicable).  
Please check the document version above.






**Copyright**

Other than for strictly personal use, it is not permitted to download, forward or distribute the text or part of it, without the consent of the author(s) and/or copyright holder(s), unless the work is under an open content license such as Creative Commons.

**Takedown policy**

Please contact us and provide details if you believe this document breaches copyrights.  
We will remove access to the work immediately and investigate your claim.

# Anharmonicity in bcc refractory elements: A detailed *ab initio* analysis

Prashanth Srinivasan <sup>1,2</sup>, Alexander Shapeev <sup>3</sup>, Jörg Neugebauer <sup>4</sup>, Fritz Körmann <sup>2,4</sup> and Blazej Grabowski <sup>1</sup>

<sup>1</sup>*Institute for Materials Science, University of Stuttgart, Pfaffenwaldring 55, 70569 Stuttgart, Germany*

<sup>2</sup>*Department of Materials Science and Engineering, Delft University of Technology, 2628 CD Delft, The Netherlands*

<sup>3</sup>*Skolkovo Institute of Science and Technology, Skolkovo Innovation Center, Nobel Street 3, Moscow 143026, Russia*

<sup>4</sup>*Max-Planck-Institut für Eisenforschung GmbH, 40237 Düsseldorf, Germany*



(Received 16 September 2022; accepted 6 December 2022; published 4 January 2023)

Explicit anharmonicity, defined as the vibrational contribution beyond the quasiharmonic approximation, is qualitatively different between the group V and group VI bcc refractory elements. Group V elements show a small and mostly negative anharmonic entropy, whereas group VI elements have a large positive anharmonic entropy, strongly increasing with temperature. Here, we explain this difference utilizing highly accurate anharmonic free energies and entropies from *ab initio* calculations for Nb and Ta (group V), and Mo and W (group VI). The numerically calculated entropies are in agreement with prior experimental data. The difference in behavior between the two sets of elements arises not from their high-temperature behavior but rather from the 0 K quasiharmonic reference state. We understand this by analyzing the 0 K and the high-temperature phonon density of states and the electronic density of states. The qualitative difference disappears when the anharmonicity is instead referenced with a high-temperature effective harmonic potential. However, even for an optimized effective harmonic reference, the remaining effective anharmonicity is significant. The reason is that the anharmonicity in the bcc systems—carried by asymmetric distributions in the nearest neighbors—can never be accounted for by a harmonically restricted potential.

DOI: [10.1103/PhysRevB.107.014301](https://doi.org/10.1103/PhysRevB.107.014301)

## I. INTRODUCTION

A dominant contribution to the thermodynamics of materials is provided by atomic vibrations. The *de facto* standard to account for vibrations is the quasiharmonic (QH) approximation [1,2]. However, the QH approximation neglects phonon-phonon interactions which are known to critically affect thermodynamic properties at high temperatures [3,4]. Based on recent developments, it is now possible to efficiently compute the contribution of phonon-phonon interactions beyond the QH approximation—also known as “explicit anharmonicity”—to thermodynamic potentials to high precision within an *ab initio* framework [5–7].

In earlier literature [8], explicit anharmonicity was considered negligible for fcc materials. Only with the recent, advanced techniques, the significance of anharmonic free energies for a number of fcc systems has been shown. Glensk *et al.* [9] performed a systematic study of the anharmonic contribution on a wide range of fcc metals using thermodynamic integration. All fcc metals showed a positively increasing anharmonic contribution to the free energy with increasing temperature. The anharmonicity in the close-packed metals is carried mostly by the interaction of the nearest neighbors. In particular, the distribution of the first nearest neighbor is strictly asymmetric along the nearest-neighbor direction and cannot be captured by a harmonic potential, neither a 0 K nor a high-temperature effective harmonic potential [9].

In comparison to fcc systems, bcc systems are expected to have much higher anharmonicity owing to their more open

crystal structure. The anharmonicity manifests not only in the first nearest neighbors but in multiple nearest neighbors in the system. In fact, the significantly higher anharmonic contribution to the free energy has been shown in various bcc systems. For example, the fully anharmonic contribution was included in the free-energy calculations for bcc Nb [7]. Similar results were also observed for more complex bcc systems such as refractory high entropy alloys [10,11], where neglecting the anharmonic contribution significantly affects the calculated thermodynamic properties.

In a work performed several years ago [12,13], an experimental determination of the explicit anharmonic entropy (aided by theoretical models) was performed for several transition metals. In their work, Eriksson *et al.* [12] calculated the anharmonic entropy by subtracting the electronic and QH entropy from the total entropy. The total entropy was obtained from experimental heat capacities, the QH entropy from neutron scattering experimental data, and the electronic entropy using the linear muffin tin orbital approach. Unlike fcc systems that are qualitatively consistent in their trend in the anharmonic entropies, critical differences were noticed within the bcc metals. The experimentally calculated explicit anharmonic entropies from Ref. [12] are displayed in Fig. 1 for the bcc refractory metals at the respective melting points. Specifically, the group V elements show a small and mostly negative anharmonic entropy (with the exception of vanadium which is predominantly small and negative but becomes small and positive at temperatures near the melting point). On the other hand, the group VI elements, with an additional valence

IV		V		VI		VII	
22	Ti	23	V +0.15	24	Cr +0.82	25	Mn
40	Zr	41 2741K Nb -0.10	42 2890K Mo +0.55	43	Tc		
72	Hf	73 3269K Ta -0.09	74 3680K W +0.48	75	Re		

FIG. 1. Experimentally calculated explicit anharmonic entropies (in  $k_B$ ) (bottom right) at the melting point (top right) for group V and group VI elements from Ref. [12]. The four refractory elements studied in this paper are colored in blue and orange.

electron, show a large and positive anharmonic entropy that increases with temperature. The difference in the explicit anharmonicity between the group V and group VI bcc refractory elements is not thoroughly explained in the literature.

In the present paper, we use *ab initio*-based techniques to understand this difference. We restrict our analysis to the four refractory elements: Nb and Ta from group V (colored in blue in Fig. 1) and Mo and W from group VI (colored in orange). First, we calculate highly accurate anharmonic free energies and entropies. By using a 0 K QH potential as the reference, we make a direct comparison to the existing experimental results. We find good resemblance in the explicit anharmonic entropy, with our current results being much more accurate owing to the state-of-the-art methodology. Most importantly, Nb and Ta show a different trend compared to Mo and W. We compare the 0 K and high-temperature phonon density of states (pDOS) and the electronic density of states (eDOS) and conclude that the difference in behavior comes from the difference in the 0 K QH reference potential used as the reference for defining explicit anharmonicity. In addition to the 0 K QH reference, we also perform anharmonic calculations with a high-temperature effective harmonic reference [14]. All the four refractory elements show a qualitatively similar trend in the resulting “effective anharmonicity.” However, there is nevertheless a considerable effective anharmonic free-energy contribution at high temperatures even when the high-temperature effective harmonic potential is used as a reference.

## II. METHODOLOGY AND COMPUTATIONAL DETAILS

The vibrational free-energy contribution  $F^{\text{vib}}$  to the total Helmholtz energy comes from phonons and the interaction between phonons, and is conventionally decomposed into a harmonic and an anharmonic part. When the harmonic part is defined using the 0 K QH approximation corresponding to noninteracting, volume-dependent 0 K phonons (free

energy labeled as  $F^{\text{qh-0K}}$ ), the resulting anharmonicity coming from phonon-phonon interactions is referred to as the “explicit anharmonicity” ( $F^{\text{ah-expl}}$ ). The harmonic part can also be defined using high-temperature effective harmonic phonons ( $F^{\text{qh-eff}}$ ) [14,15]. In such a case, we refer to the resulting anharmonicity as “effective anharmonicity” ( $F^{\text{ah-eff}}$ ). We can thus write

$$F^{\text{vib}}(V, T) = F^{\text{qh-0K}}(V, T) + F^{\text{ah-expl}}(V, T) \quad (1)$$

$$= F^{\text{qh-eff}}(V, T) + F^{\text{ah-eff}}(V, T), \quad (2)$$

with  $V$  the volume and  $T$  the temperature. Note that the resulting vibrational free energy is not affected by the way we split between the two contributions.

To calculate the explicit and the effective anharmonic free energy, we perform thermodynamic integration using a 0 K QH and a high-temperature effective harmonic reference, respectively. We use the most recent version of a methodology to compute high-accuracy vibrational free energies—the direct upsampling technique [7]. For each of the four elements, for a set of volume and temperature points, a thermodynamic integration is performed from the reference to an optimized machine-learning potential, specifically a moment tensor potential (MTP). Following this, snapshots generated by the MTP are chosen and energies are calculated using density functional theory (DFT) to obtain the free-energy difference within the free-energy perturbation theory. Summing up the two contributions gives the anharmonic free energy

$$F^{\text{ah}}(V, T) = \Delta F^{\text{ref} \rightarrow \text{MTP}}(V, T) + \Delta F^{\text{up}}(V, T), \quad (3)$$

where  $F^{\text{ah}}(V, T)$  is the explicit anharmonic free energy  $F^{\text{ah-expl}}(V, T)$  when  $\text{ref} = \text{qh-0K}$  and the effective anharmonic free energy  $F^{\text{ah-eff}}(V, T)$  when  $\text{ref} = \text{qh-eff}$ . Further in Eq. (3),  $\Delta F^{\text{ref} \rightarrow \text{MTP}}$  represents the free energy obtained by thermodynamic integration from the reference to MTP, and  $\Delta F^{\text{up}}$  is the free-energy perturbation term obtained by upsampling from MTP to DFT. The anharmonic entropy is obtained by calculating the numerical derivative of the free energy with temperature.

### A. QH reference

The 0 K QH reference free energy is calculated from the 0 K phonon frequencies for each volume [2]. The phonon frequencies are calculated using the finite-displacement method [16]. Forces on the displaced structure are calculated with DFT using VASP [17,18], with the projector augmented-wave (PAW) potentials [19] and the generalized gradient approximation (GGA) [20–22]. We use a 125-atom cell with an energy cutoff of 500 eV, an  $8 \times 8 \times 8$   $k$ -point mesh, and the reciprocal space sampled with a Methfessel-Paxton smearing scheme [23] with a smearing width of 0.1 eV.

### B. ILDOS analysis

The 0 K force constants obtained using the QH approximation are corroborated with a real-space analysis of the charge densities. Specifically, we use the integrated local density of states (ILDOS) which is the summation of all electronic states

in a given energy window,

$$\text{ILDOS}(r) = \int_{\varepsilon_1}^{\varepsilon_2} \sum_i |\psi_i(r)|^2 \delta(E_i - \varepsilon) d\varepsilon,$$

where  $(\varepsilon_1, \varepsilon_2)$  is the energy window and  $\psi_i(r)$  is the  $i$ th wave function with energy  $E_i$ . We track the change in the ILDOS in a 125-atom supercell when a single atom in the ideal structure is displaced along the [100] direction by 0.02 Å (within the QH regime). We choose an energy window of  $\pm 0.1$  eV around the Fermi level to calculate the change in the ILDOS.

### C. Effective harmonic reference

The effective harmonic force constants at the different volumes are obtained by fitting to the corresponding high-temperature *ab initio* molecular dynamics (AIMD) forces [15,24] using the SPHINX code [25]. The AIMD runs are performed with VASP using 125-atom supercells with an energy cutoff of 400 eV and a  $2 \times 2 \times 2$   $k$ -point mesh for 1000 steps each and a time step of 5 fs. From the effective harmonic force constants, the total energies of the configurations during the thermodynamic integration are analytically calculated.

### D. MTP fitting

We fit an MTP for each of the elements using the MLIP code [26,27]. A level-20 MTP is fit to AIMD data. The MTP has 329 parameters and a radial cutoff of 5 Å (up to the third neighbor shell). The training set is obtained from  $NVT$  (canonical ensemble) AIMD runs performed with VASP in 125-atom supercells at 3000 K and at six volumes. At each fixed volume, the temperature is maintained using a Langevin thermostat with a friction parameter of 0.01 fs<sup>-1</sup>. The relevant volume range at 3000 K is chosen based on the Debye-Grüneisen approximation [28] from an energy-volume curve. The AIMD runs are performed with an energy cutoff of 400 eV and a  $2 \times 2 \times 2$   $k$ -point mesh for 1000 steps each and a time step of 5 fs. From the AIMD runs, uncorrelated snapshots (one in every ten configurations) are chosen to train an initial MTP. In the next round, additional snapshots are chosen by utilizing this initially trained MTP and are added to the training set to retrain and obtain the final MTP. The root-mean-square errors (RMSEs) in energy and forces of the final MTPs are in the range 1-2 meV/atom and 0.12–0.16 eV/Å, respectively.

### E. Thermodynamic integration with direct upsampling

As the first step of the direct upsampling methodology [7], we perform thermodynamic integration ( $\lambda$  integration) from the reference (0 K QH or effective harmonic) to MTP. Eight to ten temperatures up to the melting point and 11 volumes at each temperature are chosen. At each  $(V, T)$  point, thermodynamic integration is run with 22  $\lambda$  values ( $0 \leq \lambda \leq 1$ ) for 30 000 steps each with a time step of 2 fs. The numerically calculated area under the internal energy difference curve with  $\lambda$  gives the free-energy difference between the reference and MTP at each  $(V, T)$  [ $\Delta F^{\text{ref} \rightarrow \text{MTP}}(V, T)$  in Eq. (3)].

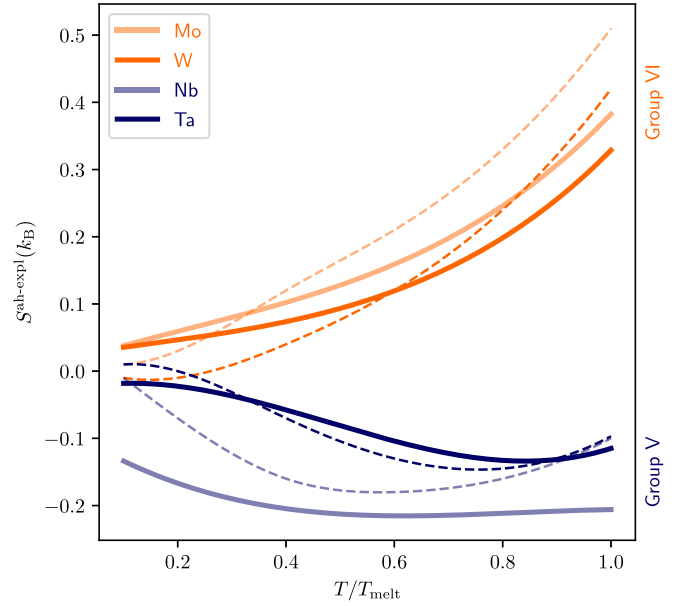


FIG. 2. Comparison of the *ab initio*-calculated explicit anharmonic entropies for the four studied elements (in solid lines) with previous experimental values (in dashed lines). The experimental curves are reproduced from Ref. [12].

Next, we choose uncorrelated snapshots generated by the MTP at each  $(V, T)$ . We calculate the DFT energies of these configurations using high-precision parameters [the same parameters as used for the 0 K forces (Sec. II A)]. The upsampled energy [ $\Delta F^{\text{up}}(V, T)$  in Eq. (3)] is calculated using the free-energy perturbation expression [29,30] as given by

$$\Delta F^{\text{up}} = -k_B T \ln \left\langle \exp \left( -\frac{E^{\text{DFT}} - E^{\text{MTP}}}{k_B T} \right) \right\rangle_{\text{MTP}}, \quad (4)$$

where  $E^{\text{DFT}}$  and  $E^{\text{MTP}}$  are internal energies calculated using DFT and MTP, respectively, and the averaging is done over configurations generated by the MTP. The upsampled free energy is calculated using 24 snapshots within which the value is converged to within 1 meV/atom. At each  $(V, T)$ , the total anharmonic free energy  $F^{\text{ah}}(V, T)$  is obtained by summing the upsampled energy  $\Delta F^{\text{up}}(V, T)$  with the free-energy difference calculated in the previous thermodynamic integration stage  $\Delta F^{\text{ref} \rightarrow \text{MTP}}(V, T)$ . Using these values of  $F^{\text{ah}}(V, T)$ , a smooth higher-order polynomial surface is parametrized in volume and temperature.

## III. RESULTS AND DISCUSSION

Figure 2 shows the explicit anharmonic entropies (using the 0 K QH reference) up to the melting point for the four bcc refractory elements. The *ab initio*-computed values (solid lines) are compared to the previously existing experimental data (dashed lines). Our current results from first principles show a good qualitative and quantitative resemblance to the experimental data. The minor differences between the current *ab initio* and prior experimental results can have the following sources. First, the experimental data could contain measurement errors in the heat capacities (which are difficult to measure at high temperatures) or in the phonon

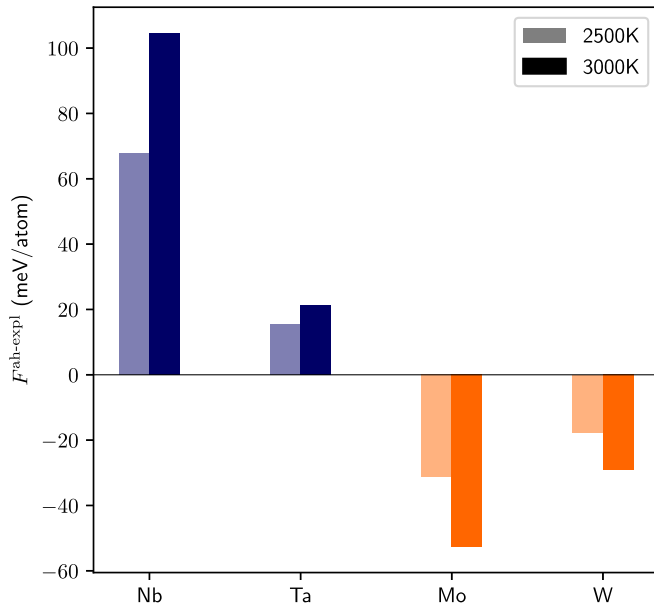


FIG. 3. *Ab initio*-calculated explicit anharmonic vibrational free energies for the four elements at 2500 and 3000 K and at the corresponding equilibrium volumes.

frequencies from neutron scattering. On the theoretical side, an inherent approximation is the exchange-correlation functional, although for Nb, the here employed GGA functional was shown to predict very accurate high-temperature thermodynamic properties [7]. Further, in the experimental work, Eriksson *et al.* [12] obtained the anharmonic entropy by removing the electronic and the QH entropy from the total entropy. Importantly, the temperature-dependent electronic entropy was obtained on a fixed static lattice, and the authors [12] did not consider the change in the electronic energies coming from phonons which is significant in these systems [31]. Nevertheless, we see that the different behavior of the group V elements Nb and Ta (colored in blue in Fig. 2) as compared to the group VI elements Mo and W (colored in orange) is clearly captured by both the current theoretical results and the existing experimental data.

Nb and Ta exhibit a small negative anharmonic entropy with a comparably weak temperature dependence, whereas Mo and W exhibit a large and positive explicit anharmonic entropy that increases with increasing temperature. The values are almost double in magnitude for Mo and W at temperatures near the melting point. A clear difference between the group V and group VI elements is also noticed in the explicit anharmonic free energies. In Fig. 3, we demonstrate the explicit anharmonic free energies at 2500 and 3000 K at the respective equilibrium volumes. Nb and Ta show positive explicit anharmonic free energies, whereas Mo and W show negative values. The magnitude of the explicit anharmonic free energies at 2500 and 3000 K is in the range 20–100 meV/atom indicating that the bcc refractory elements are appreciably more anharmonic in comparison to fcc unaries, whose values were less than 25 meV/atom at the melting point [9].

To understand the difference in behavior between the group V and group VI refractory elements, we analyze the phonons corresponding to the 0 K QH and the 3000 K effective har-

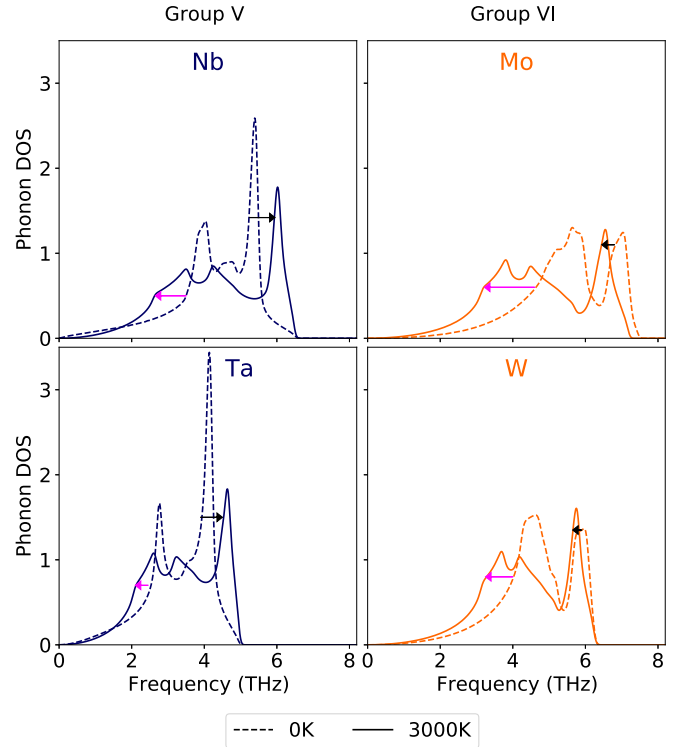


FIG. 4. Comparison of the pDOS calculated from the 0 K QH force constants (dashed) and the 3000 K effective harmonic force constants (solid). The magenta and black arrows represent the shift in the low-energy and high-energy branches of the phonon modes, respectively.

monic potential. Figure 4 comprises the results with the 0 K phonon DOS plotted in dashed lines and the 3000 K phonon DOS in solid lines. The temperature-induced shifts in the low-energy phonon modes are indicated by the magenta arrows, whereas the changes in the high-energy modes are highlighted by the black arrows. The low-energy branches generally represent long-range strain interactions in the crystal, whereas the high-energy branches represent more localized interactions.

There is no qualitative difference in trend in the low-energy phonon modes. For all the four elements, these modes become softer at 3000 K, albeit with a more pronounced reduction in Mo and W. A clearer, qualitative difference in trend occurs in the high-energy branches. In the group VI elements of Mo and W, similarly to the low-energy modes, the high-energy branches of the renormalized phonons at 3000 K become softer, as compared to the stiff phonons at 0 K. The softening is gradual with increasing temperature. The renormalization and softening of both the low-energy and high-energy phonon modes at higher temperatures is reflected in the negative explicit anharmonic free energies and the positive anharmonic entropies, both of which are also observed to increase in magnitude with temperature. In contrast, the high-energy branches of the 0 K phonons in Nb and Ta are softer, and the renormalized high-temperature phonons are stiffer at 3000 K. The renormalization and the hardening of the high-energy phonons with temperature thus has an opposite effect on the explicit anharmonic free energies and entropies in Nb and Ta. Based on these results, we can already speculate that the opposite



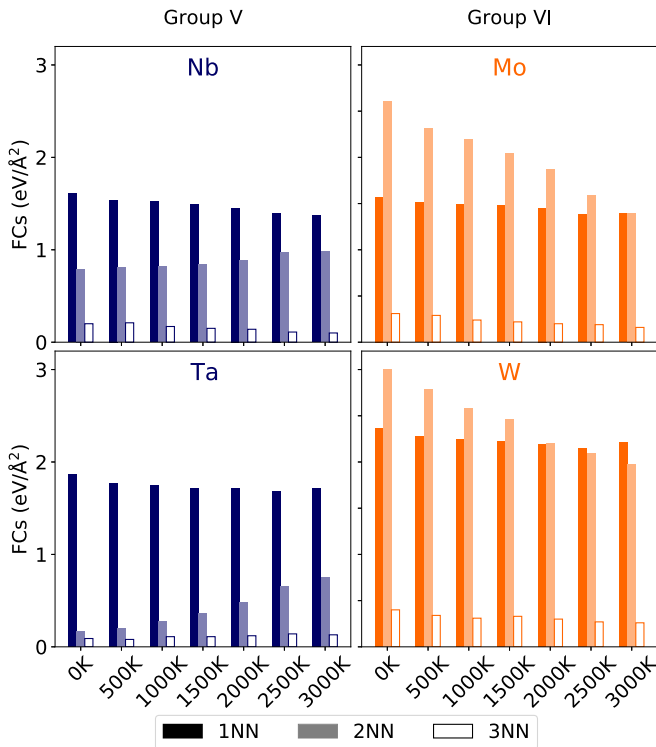


FIG. 5. First, second, and third nearest-neighbor force constants (FCs) at different temperatures for all four studied elements. The 0 K force constants are from the QH approximation, whereas the higher-temperature force constants are obtained by fitting an effective harmonic potential to MD data at the corresponding temperature and volume.

trends in the explicit anharmonicity between the group V and group VI elements are, in fact, an artifact of the behavior of the 0 K QH reference.

In addition to the phonon DOS, we also demonstrate the effect of temperature on the nearest-neighbor force constants. The 0 K force constants are obtained from the 0 K QH approximation, and the force constants at higher temperatures are obtained from the effective harmonic models at the corresponding temperature and volume. The first three nearest-neighbor force constants are shown in Fig. 5 up to 3000 K. The softer phonons at 0 K and the phonon hardening with temperature exhibited by Nb and Ta and the opposite trend in Mo and W (Fig. 4) are also reflected in the nearest-neighbor force constants, especially along the second nearest-neighbor (2NN) direction. At 0 K, Mo and W possess much higher 2NN force constants which decrease monotonously with temperature. The effect is opposite in Nb and Ta where the 2NN force constants increase monotonously with temperature. The increased effect of smearing and atomic vibrations as the temperature increases in the bcc refractory elements brings the first and second nearest-neighbor force constants closer to each other. As observed, the effect is negligible for the third nearest neighbor, which is much farther away.

The difference in the 0 K force constants behavior exhibited by the four elements for the 2NN interaction can be corroborated by a real-space charge density analysis. Fig-

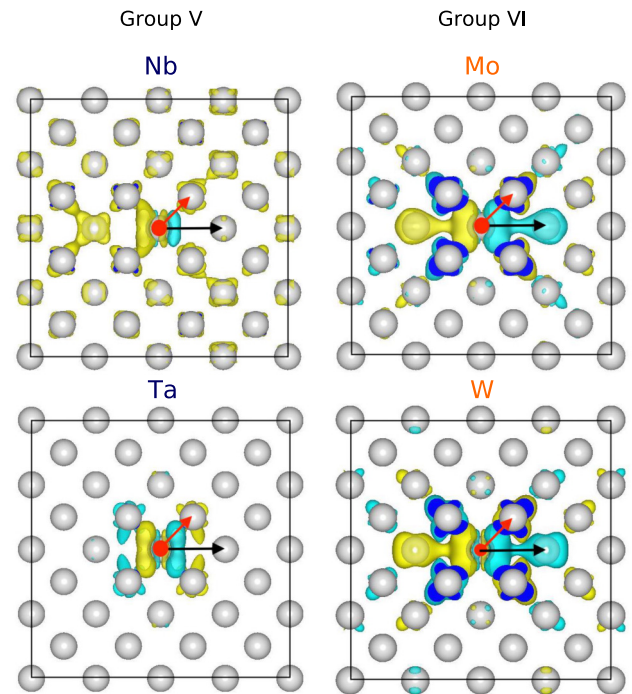


FIG. 6. Change in ILDOS when an atom is displaced by  $0.015 \text{ \AA}$  towards the 2NN relative to the ideal structure projected along the (001) plane. The isosurface value of the ILDOS has been optimized for best visualization. Yellow and blue are negative and positive values of the change in ILDOS, respectively.

ure 6 shows the isosurface of the change in ILDOS for the four refractory elements projected on the (100) plane. The central atom, shown in red, is the displaced atom during the analysis. The red and black arrows indicate the 1NN and 2NN directions, respectively. We notice that the dominant distortion of the ILDOS is only along the 1NN (along the red arrow) in Nb and Ta, whereas there is an additional large distortion also along the 2NN (along the black arrow) for Mo and W. There is a correlation between the distortion in ILDOS along a particular nearest-neighbor direction and the force constant along that particular neighbor, with Mo and W being stiffer and having additionally a large 2NN-oriented force constant at 0 K (Fig. 5).

The difference in explicit anharmonicity between Nb/Ta and Mo/W at 0 K can be also traced back to the electronic density of states (eDOS), plotted in Fig. 7. In Mo and W, the Fermi level falls in a valley of the static 0 K eDOS implying that the 0 K bcc structure is rather stable and difficult to deform, and has higher-energy phonons. At higher temperatures, when the eDOS gets smeared out from thermal vibrations, the value of the eDOS at the Fermi level increases, implying a destabilization of the bcc structure with respect to 0 K. The trend is reversed in Nb and Ta, wherein the Fermi level falls closer to a peak of the 0 K eDOS, and smearing of the eDOS from thermal vibrations leads to a stabilization of the bcc structure at higher temperatures and the hardening of the high-energy branch of the phonons. Since the smeared out high-temperature eDOS for all four elements are similar, we can once again suggest that the difference in explicit

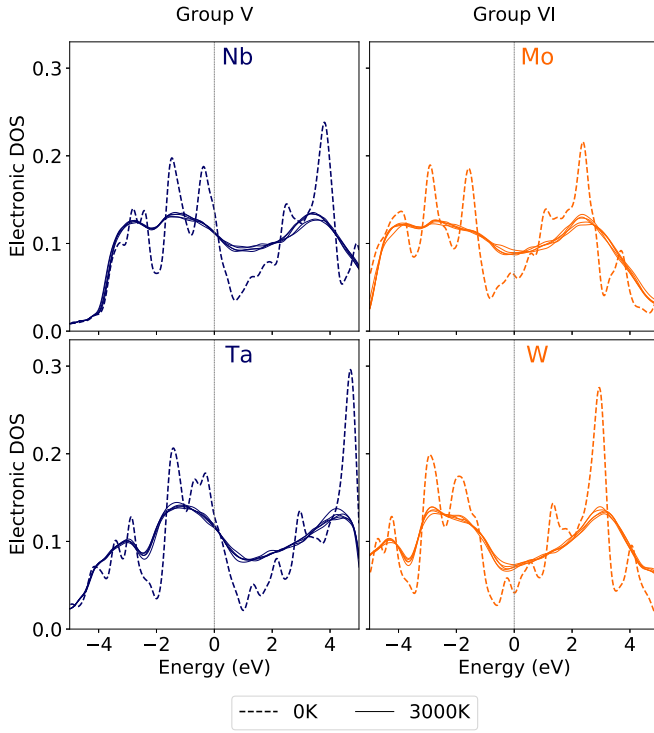


FIG. 7. Comparison of the 0 K static eDOS (dashed) and the eDOS of five random configurations from a 3000 K AIMD run (solid).

anharmonicity arises rather from the 0 K QH reference. To further verify the hypothesis, we also analyze the “effective anharmonic” free energies obtained with the high-temperature renormalized phonons (effective harmonic) as the reference. In Fig. 8, we plot and compare the effective anharmonic free energies at 2500 and 3000 K. At each temperature, we use an effective harmonic potential that is fitted to the AIMD data at that particular temperature and the corresponding equilibrium volume. We observe that the effective anharmonic free energies are both qualitatively and quantitatively similar, with values ranging from 9 to 25 meV/atom. Compared to the explicit anharmonic free energies, all four elements show a positive anharmonic free energy when referenced with an effective harmonic potential. Table I summarizes both the explicit and effective anharmonic free energies and entropies at 2500 and 3000 K. In addition to the similar trends in the free energies, the effective anharmonic entropies are also similar

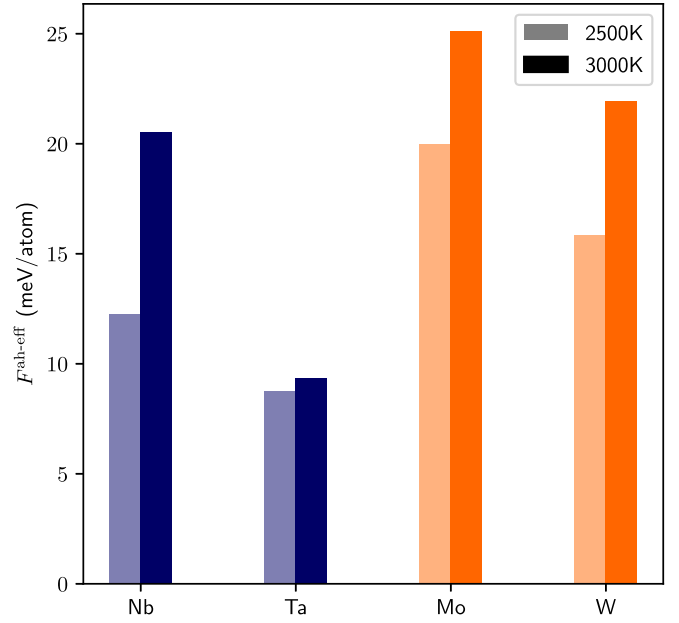


FIG. 8. *Ab initio* calculated effective anharmonic vibrational free energies at 2500 and 3000 K and at the corresponding equilibrium volumes using a consistent effective harmonic reference, i.e., fitted at the corresponding volume and temperature.

within the four refractory elements as noticed in the last two columns of the table.

In both Fig. 8 and in Table I, we observe that there is still a significant effective anharmonic free energy that is unaccounted for even though the reference effective harmonic potentials are fitted to the corresponding high-temperature forces. The effective harmonic potentials are, by construction, “harmonic” in nature and cannot exactly capture the quite significant anharmonicity in the bcc elements at high temperatures. Hence, for accurate thermodynamic property predictions, it is thus a requisite to include the effective anharmonic free energies, and it is not sufficient to approximate the vibrational free energy with high-temperature effective harmonic references.

It was shown previously [9] that the effect of anharmonicity can be predominantly captured within a localized environment. In the work of Glensk *et al.* [9], the anharmonicity in the system was traced to anharmonicity in local first nearest-neighbor (1NN) pairwise interactions. A similar analysis can also be made in the bcc refractory elements. Figure 9 is a

TABLE I. Compilation of the explicit and effective anharmonic free energies and entropies for the four studied refractory elements at 2500 and 3000 K and at the corresponding equilibrium volumes.

	0 K QH				Effective QH at consistent $V$ and $T$			
	$F^{\text{ah-expl}}$ (meV/atom)		$S^{\text{ah-expl}}$ ( $k_B$ )		$F^{\text{ah-eff}}$ (meV/atom)		$S^{\text{ah-eff}}$ ( $k_B$ )	
	2500 K	3000 K	2500 K	3000 K	2500 K	3000 K	2500 K	3000 K
Nb	67.95	104.55	−0.20	−0.19	12.24	20.54	−0.07	−0.07
Ta	15.47	21.33	−0.12	−0.13	8.76	9.33	−0.13	−0.11
Mo	−31.28	−52.67	0.29	0.39	19.98	25.10	−0.15	−0.08
W	−17.69	−29.17	0.14	0.20	15.83	21.91	−0.15	−0.11

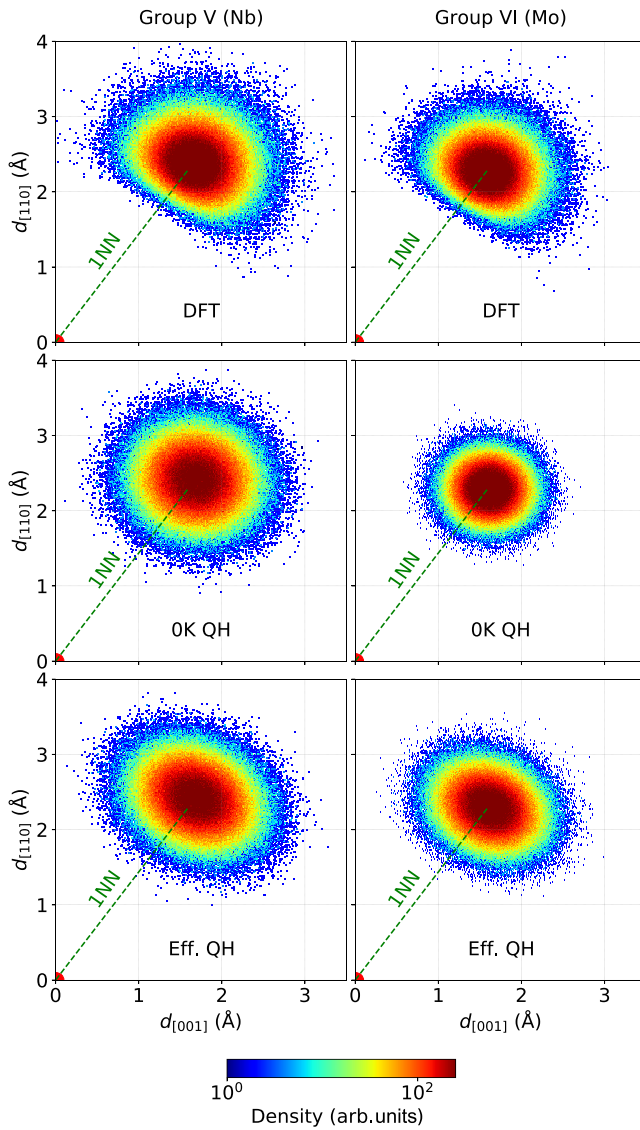


FIG. 9. First nearest-neighbor distribution in Nb and Mo at 3000 K and at the corresponding equilibrium volume based on DFT AIMD, 0 K QH, and 3000 K effective harmonic potentials.

two-dimensional (2D) representation of the 1NN distribution in Nb and Mo with the center of reference at (0,0). Here, the projections of the 1NN vector on the (110) plane are shown as a contour plot for an MD run at 3000 K and at the corresponding equilibrium volume using DFT, the 0 K QH, and the 3000 K effective harmonic potential, respectively. There are several key takeaways that can be made from the figure. First, one can notice the anharmonicity in the DFT plots of both Nb and Mo. There is an evident asymmetry in the distribution along the longitudinal direction (shown as a green dashed line) with a wall-like planar edge while going from the center of the distribution towards the origin at (0,0). Such an asymmetry is not observed in the 0 K QH distributions which show a characteristic symmetric shape along both the longitudinal and transversal directions. The crucial observation in the 0 K QH distributions is the difference in their size in comparison to the DFT ones. Nb shows a broader and

more widely spread 0 K QH distribution compared to DFT, whereas it is much narrower in Mo. This can be traced back to the phonon behavior discussed in Fig. 4. Nb exhibits softer phonons at 0 K that lead to a broader distribution whereas Mo exhibits much stiffer phonons at 0 K that keep the atomic displacements smaller. This further illustrates the difference in trends in explicit anharmonicity between group V and group VI refractory elements. The last row in the figure shows the 1NN distribution using the effective harmonic potential. Contrary to the 0 K QH distribution, the size of the effective harmonic distribution is similar to the corresponding DFT distributions for both Nb and Ta. Nonetheless, it is observed that the distribution is still symmetric along both directions owing to the “harmonic” nature of the model and is unable to replicate the planar-edge asymmetry of DFT. Again, this exemplifies the similarity in trends at high temperature and the impending effective anharmonic free energies while utilizing the effective harmonic model as the reference.

We also compute and analyze the Gauss-broadened 1D distribution  $\rho_{1NN}(d) = \sum_j \delta(|\vec{d}_{1NN}^j| - d)$  as a function of distance  $d$ . Here,  $\vec{d}_{1NN}^j$  represents the 1NN vector and  $j$  runs over all MD steps. This atomic distribution function is used to construct an effective 1D potential, specifically by  $v_{\text{eff}}(d) = -k_B T \ln \rho_{1NN}(d)$ . We focus on Nb and Mo at 3000 K for the analysis. The obtained distributions and effective potentials for the harmonic approximations and the fully anharmonic simulation are plotted as a function of the 1NN distance ( $d_{1NN}$ ) around the equilibrium distance ( $d_{1NN}^{\text{eq}}$ ) in the first two rows in Fig. 10. In order to emphasize the dissimilarities in the effective potentials, we also plot the differences to the full vibrational energies in the third row of the figure. The takeaways from Fig. 9 that were discussed above are also evident from Fig. 10. Both the 0 K QH and the effective harmonic curves are symmetric around the equilibrium distance, whereas the full vibrational curves are not, owing to the anharmonicity. In Nb, the 0 K QH distribution function with respect to the full vibrational distribution function is higher at shorter distances (and the effective potential is smaller) due to the softer phonons and broader 1NN distribution. The behavior is opposite in Mo. The contrast between Nb and Mo is more pronounced in the third row of the figure. It is seen that the difference of the full vibrational energy and the 0 K QH is positive as a function of the 1NN distance in Nb, whereas it is negative for Mo. On the other hand, the difference with the effective harmonic reference is similar for both Nb and Mo. Once again, it further highlights the difference in the 0 K behavior and the similarity in the high-temperature effective harmonic reference.

In addition to the 1NN, anharmonicity is carried to a smaller extent also in the second nearest neighbors (2NNs) in the bcc refractory elements. This is illustrated in Fig. 11 which shows the 2NN distribution on the (110) plane for the same MD runs as used in Fig. 9. Similar inferences can be made also from the 2NN distribution. The DFT distribution is asymmetric along the longitudinal direction—we observe a less-pronounced wall-like planar edge—while going from the center of the distribution to the reference at (0,0). The 0 K QH distribution of Nb is broader and that of Mo is smaller owing to similar reasons as discussed above. The size of the effective



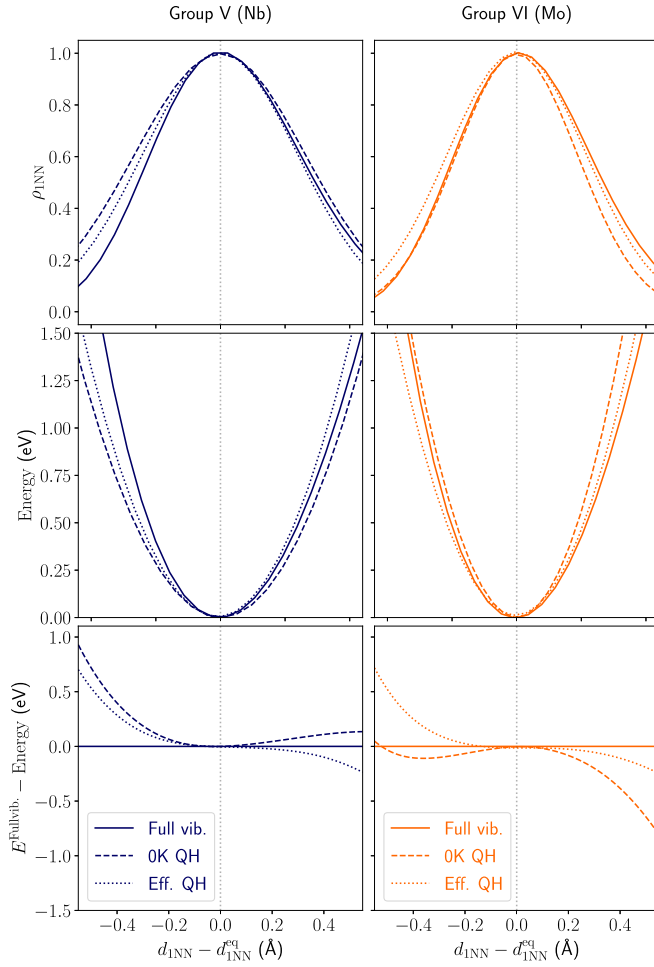


FIG. 10. Gauss-broadened first nearest-neighbor distribution function, the corresponding effective potential, and the difference in the effective potential with DFT for Nb and Mo at 3000 K at the corresponding equilibrium volume.

harmonic distribution is similar with respect to the respective DFT distributions, yet, by default symmetric in nature.

The second neighbor distributions can be used to explain the effect of temperature on the 2NN force constants discussed above (Fig. 5). In the top part of Fig. 12, we plot the 1D distribution of the second neighbor distances at 3000 K for Nb and Mo. In the same figure, we also plot the 2NN 0 K forces from DFT as a function of interatomic separation (solid lines). The black bars between  $-0.02$  and  $0.02$  Å correspond to the QH regime. The 0 K QH potentials approximate the DFT forces in this regime resulting in the linear force dependencies shown by the dashed lines. The 0 K QH forces are much steeper for Mo (higher force constants) compared to Nb. On the other hand, the effective QH potentials produce effective, linear forces (dotted lines) based on their fitting temperature. Specifically, the second neighbor distributions shown in the top part of the figure dictate the regime in which the forces are fit to at 3000 K. The distribution for Mo shows a shift towards the right (denoted by the black arrow) as compared to Nb. This leads to effective, linear forces (dotted line) for Mo that approximate the DFT forces (solid line) at positive displacements where there is the highest neighbor distribution. For Nb,

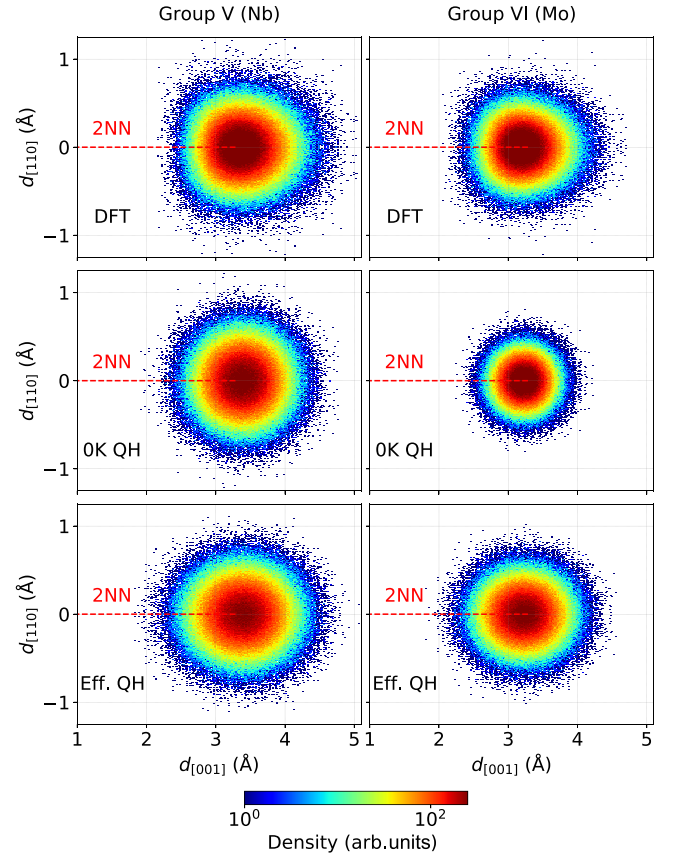


FIG. 11. Second nearest-neighbor distribution in Nb and Mo at 3000 K at the corresponding volume based on DFT AIMD, 0 K QH, and 3000 K effective harmonic potentials.

the relative displacements are smaller and slightly negative in the regime with maximum distribution where the effective QH approximates the DFT forces linearly. As a consequence, the effective high-temperature 2NN force constant (obtained

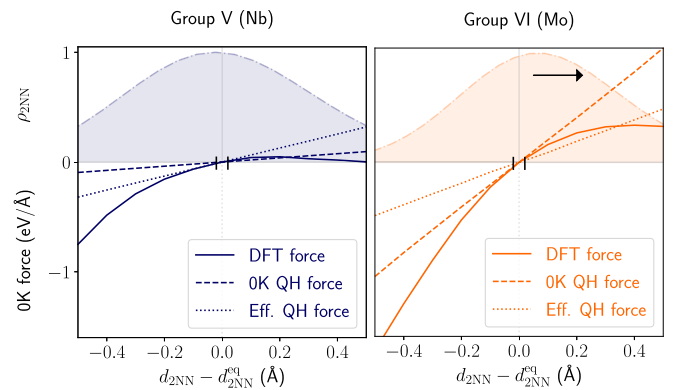


FIG. 12.  $T = 0$  K forces as a function of second neighbor displacement predicted by DFT (solid line), the 0 K QH (dashed line), and the 3000 K effective harmonic potential (dotted line) for Nb and Mo. Top part: The Gauss-broadened second neighbor distribution function ( $\rho_{2NN}$ ; dashed line and shading) during a DFT run at 3000 K and equilibrium volume. The black arrow signifies a shift in the distribution in Mo (group VI).

from the effective QH) in Mo becomes smaller than at 0 K, and the effect is reversed in Nb. The strong nonlinearity of the DFT forces as a function of displacement again reflects clearly the significant anharmonicity that cannot be captured by any linear force dependence, i.e., harmonic potential, whether 0 K or effective.

The above discussion of Figs. 9–12, for Nb and Mo also holds true for Ta and W.

#### IV. CONCLUSIONS

We have computed *explicit* anharmonic free energies and entropies for Nb, Mo, Ta, and W. The previously known experimental information about the difference in trends between the group V and group VI bcc refractory elements has been confirmed and explained in detail using the *ab initio*-computed values. The difference in the explicit anharmonic values between Nb and Ta in comparison to Mo and W arises, not from the high-temperature behavior, but rather from the 0 K behavior. Temperature destabilizes the bcc structure of Mo and W, whereas it stabilizes bcc Nb and Ta. In the bcc refractory elements, the anharmonic behavior manifests itself predominantly in the first nearest neighbors and also in the second neighbors.

Additionally, we have also calculated *effective* anharmonic free energies utilizing a high-temperature effective harmonic reference. Unlike the explicit anharmonicity, the effective anharmonicity is consistent across all the refractory elements. Nevertheless, there is still a considerable effective anharmonicity in all four systems. Highly anharmonic systems such as refractory elements cannot be represented

accurately with a restricted “harmonic” model, even if fitted to high-temperature data. Although such “effective” harmonic potentials are powerful in representing high-temperature vibrational behavior, in order to reach DFT accuracy, they are insufficient and one needs to resort to more accurate models (such as, e.g., machine-learning-based potentials). Failing to do so can have a significant effect on numerical high-temperature thermodynamic property prediction, for instance, in highly anharmonic refractory high entropy alloy systems.

#### ACKNOWLEDGMENTS

We appreciate fruitful discussions regarding ILDOS with Liang-Feng Huang. P.S. would like to thank the Alexander von Humboldt Foundation for their support through the Alexander von Humboldt Postdoctoral Fellowship Program. This project has received funding from the European Research Council (ERC) under the European Union’s Horizon 2020 research and innovation programme (Grant Agreement No. 865855). F.K. and B.G. acknowledge support from the collaborative DFG-RFBR Grant (Grants No. DFG KO 5080/3-1 and No. DFG GR 3716/6-1). B.G. acknowledges the support by the Stuttgart Center for Simulation Science (SimTech). F.K. acknowledges support by the DFG under the priority program 2006 “CCA - HEA” and by the Nederlandse Organisatie voor Wetenschappelijk Onderzoek (NWO) (VIDI Grant No. 15707). A.S. acknowledges support from the collaborative DFG-RFBR Grant (Grant No. RFBR 20-53-12012). J.N. acknowledges support by the DFG (German Research Foundation) under Projects No. 405621160 and No. 405621217.

- 
- [1] K. Kunc and R. M. Martin, *Ab Initio* Force Constants of GaAs: A New Approach to Calculation of Phonons and Dielectric Properties, *Phys. Rev. Lett.* **48**, 406 (1982).
  - [2] K. Parlinski, Z. Q. Li, and Y. Kawazoe, First-Principles Determination of the Soft Mode in Cubic ZrO<sub>2</sub>, *Phys. Rev. Lett.* **78**, 4063 (1997).
  - [3] B. Grabowski, P. Söderlind, T. Hickel, and J. Neugebauer, Temperature-driven phase transitions from first principles including all relevant excitations: The fcc-to-bcc transition in Ca, *Phys. Rev. B* **84**, 214107 (2011).
  - [4] A. Glensk, B. Grabowski, T. Hickel, and J. Neugebauer, Breakdown of the Arrhenius Law in Describing Vacancy Formation Energies: The Importance of Local Anharmonicity Revealed by *ab initio* Thermodynamics, *Phys. Rev. X* **4**, 011018 (2014).
  - [5] A. I. Duff, T. Davey, D. Korbacher, A. Glensk, B. Grabowski, J. Neugebauer, and M. W. Finnis, Improved method of calculating *ab initio* high-temperature thermodynamic properties with application to ZrC, *Phys. Rev. B* **91**, 214311 (2015).
  - [6] B. Grabowski, Y. Ikeda, P. Srinivasan, F. Körmann, C. Freysoldt, A. I. Duff, A. Shapeev, and J. Neugebauer, *Ab initio* vibrational free energies including anharmonicity for multicomponent alloys, *npj Comput. Mater.* **5**, 80 (2019).
  - [7] J. H. Jung, P. Srinivasan, A. Forslund, and B. Grabowski, High-accuracy thermodynamic properties to the melting point from *ab initio* calculations aided by machine-learning potentials, *arXiv:2212.10385*.
  - [8] A. Khellaf, A. Seeger, and R. M. Emrick, Quenching studies of lattice vacancies in high-purity aluminium, *Mater. Trans.* **43**, 186 (2002).
  - [9] A. Glensk, B. Grabowski, T. Hickel, and J. Neugebauer, Understanding Anharmonicity in fcc Materials: From its Origin to *ab initio* Strategies beyond the Quasiharmonic Approximation, *Phys. Rev. Lett.* **114**, 195901 (2015).
  - [10] A. Ferrari, B. Dutta, K. Gubaev, Y. Ikeda, P. Srinivasan, B. Grabowski, and F. Körmann, Frontiers in atomistic simulations of high entropy alloys, *J. Appl. Phys.* **128**, 150901 (2020).
  - [11] Y. Zhou, P. Srinivasan, F. Körmann, B. Grabowski, R. Smith, P. Goddard, and A. I. Duff, Thermodynamics up to the melting point in a TaVCrW high entropy alloy: Systematic *ab initio* study aided by machine learning potentials, *Phys. Rev. B* **105**, 214302 (2022).
  - [12] O. Eriksson, J. M. Wills, and D. Wallace, Electronic, quasi-harmonic, and anharmonic entropies of transition metals, *Phys. Rev. B* **46**, 5221 (1992).
  - [13] D. C. Wallace, *Thermodynamics of Crystals* (Dover, New York, 1998).
  - [14] O. Hellman, P. Steneteg, I. A. Abrikosov, and S. I. Simak, Temperature dependent effective potential method for accurate free energy calculations of solids, *Phys. Rev. B* **87**, 104111 (2013).

- [15] O. Hellman, I. A. Abrikosov, and S. I. Simak, Lattice dynamics of anharmonic solids from first principles, *Phys. Rev. B* **84**, 180301(R) (2011).
- [16] G. Kresse, J. Furthmüller, and J. Hafner, *Ab initio* force constant approach to phonon dispersion relations of diamond and graphite, *Europhys. Lett.* **32**, 729 (1995).
- [17] G. Kresse and J. Hafner, *Ab initio* molecular-dynamics simulation of the liquid-metal–amorphous-semiconductor transition in germanium, *Phys. Rev. B* **49**, 14251 (1994).
- [18] G. Kresse and J. Furthmüller, Efficient iterative schemes for *ab initio* total-energy calculations using a plane-wave basis set, *Phys. Rev. B* **54**, 11169 (1996).
- [19] P. E. Blöchl, Projector augmented-wave method, *Phys. Rev. B* **50**, 17953 (1994).
- [20] D. M. Ceperley and B. J. Alder, Ground State of the Electron Gas by a Stochastic Method, *Phys. Rev. Lett.* **45**, 566 (1980).
- [21] J. P. Perdew and A. Zunger, Self-interaction correction to density-functional approximations for many-electron systems, *Phys. Rev. B* **23**, 5048 (1981).
- [22] J. P. Perdew, K. Burke, and M. Ernzerhof, Generalized Gradient Approximation Made Simple, *Phys. Rev. Lett.* **77**, 3865 (1996).
- [23] M. Methfessel and A. T. Paxton, High-precision sampling for Brillouin-zone integration in metals, *Phys. Rev. B* **40**, 3616 (1989).
- [24] O. Hellman and I. A. Abrikosov, Temperature-dependent effective third-order interatomic force constants from first principles, *Phys. Rev. B* **88**, 144301 (2013).
- [25] S. Boeck, C. Freysoldt, A. Dick, L. Ismer, and J. Neugebauer, The object-oriented DFT program library sPHI/nX, *Comput. Phys. Commun.* **182**, 543 (2011).
- [26] A. V. Shapeev, Moment tensor potentials: A class of systematically improvable interatomic potentials, *Multiscale Model. Simul.* **14**, 1153 (2016).
- [27] I. Novikov, B. Grabowski, F. Körmann, and A. Shapeev, Magnetic Moment Tensor Potentials for collinear spin-polarized materials reproduce different magnetic states of bcc Fe, *npj Comp. Mat.* **8**, 13 (2022).
- [28] P. Debye, Zur theorie der spezifischen wärmen, *Ann. Phys.* **344**, 789 (1912).
- [29] R. W. Zwanzig, High-temperature equation of state by a perturbation method. I. Nonpolar gases, *J. Chem. Phys.* **22**, 1420 (1954).
- [30] W. F. van Gunsteren, X. Daura, and A. E. Mark, Computation of free energy, *Helv. Chim. Acta* **85**, 3113 (2002).
- [31] X. Zhang, B. Grabowski, F. Körmann, C. Freysoldt, and J. Neugebauer, Accurate electronic free energies of the 3d, 4d, and 5d transition metals at high temperatures, *Phys. Rev. B* **95**, 165126 (2017).